Journal of Materials Science: Materials in Electronics
https://doi.org/10.1007/s10854-020-03865-y

Structural, electrical, ferroelastic behavior, and multiferroic properties of $BiFeO_3$

Muniyandi Muneeswaran[1] · Ali Akbari-Fakhrabadi[1] · Miguel Angel Gracia-Pinilla[2] · Juliano C. Denardin[3]

Received: 2 March 2020 / Accepted: 24 June 2020

Abstract
$BiFeO_3$ was synthesized by conventional solid-state reaction method, and its structural, vibrational, electrical, ferroelastic, and multiferroic properties were studied. X-ray diffraction analysis and Rietveld refinement confirmed its rhombohedral crystal structural with the space group of *R3c*. SEM images show the rectangular shaped micrograins. The stress–strain curves obtained from uniaxial compressive tests with different maximum stresses exhibit hysteresis loops with different remnant strains due to ferroelastic domain switching during compression loading and partial domain switching back upon unloading. From Raman spectra, we have observed $3A_1$ and 6E modes in the range of 100–600 cm^{-1}. Dielectric constant and dielectric loss were measured as a function of frequency in the range 100 Hz to 1 MHz. The leakage current density was found to be 8.07×10^{-7} A/cm^2 at higher electric field. In further, we performed the ferroelectric, magnetic, and magnetoelectric effect for the confirmation of its multiferroic behavior.

1 Introduction

In the past few years, much attention has been focused on multiferroic materials as they exhibit both electric and magnetic ordering in single phases. These materials have been widely studied in recent years because of their potential applications in developing new spintronic devices, memory elements and magnetic field sensors. Magnetoelectric effect is the coexistence and coupling of ferroelectricity and ferromagnetism [1]. Among studied multiferroic perovskite oxides such as $BiFeO_3$ (BFO), $TbMnO_3$, $LuFeO_3$ $YMnO_3$, $EuTiO_3$, $BiMnO_3$ [2–7], BFO is the only known perovskite oxide which exhibits both ferroelectricity and magnetism above room temperature. It has distorted rhombohedral perovskite structure with the space group of *R3c* [8] with high Curie temperature (ferroelectric ordering $T_C \sim 830$ °C) and Neel temperature (magnetic ordering $T_N \sim 370$ °C), which has made it very attractive for potential technologies. Synthesis of pure BFO compound is difficult as impurity phases such as Bi_2O_3, $Bi_2Fe_4O_3$ and $Bi_{25}FeO_{39}$ are formed due to the kinetics of phase formation [9]. Sverre M. Selbach et al. [10] reported that the several new chemical components may lead to coexistence of $BiFeO_3$, $Bi_2Fe_4O_9$, and $Bi_{25}FeO_{39}$ phases, which can be explained by the Gibbs energy of reaction. Liu et al. [11] reported that the $Bi_{25}FeO_{40}$, $Bi_{36}Fe_2O_{57}$, and $Bi_2Fe_4O_9$ secondary phases are formed at high temperatures between 650 ºC and 850 ºC along with BFO phase. These secondary phases are created some drawbacks such as (i) the reduction of Fe^{3+} to Fe^{2+} during sintering and the creation of oxygen vacancies for the charge compensation leading to the higher leakage current density [12], (ii) leading to the difficulties in obtaining saturated polarization hysteresis loop and a high remenant polarization at room temperature [13]. However, these drawbacks can be overcome by adding excess amount of Bi for the synthesis and also by doping of Bi^{3+} with rare earth metal ions [14] or Fe^{3+} with transition metal ions [15]. Various methods have been reported for the synthesis of BFO such as solid-state reaction [16], sol gel [17], autocombustion [18], and hydrothermal [19] methods. The ferroic polycrystalline perovskites consist of submicron nanograins or micron size grains which covered with the

✉ Muniyandi Muneeswaran
munisphysics@gmail.com

✉ Ali Akbari-Fakhrabadi
aliakbarif@uchile.cl

[1] Advanced Materials Laboratory, Department of Mechanical Engineering, University of Chile, Santiago, Chile

[2] Universidad Autónoma de Nuevo León, Faculated de Ciencias Fisico-Matemáticas, Av. Universidad, Cd.Universitian, N.L. C.P 66450 San Nicolás de los Graza, Mexico

[3] Department of Physics, University of Santiago, CEDENNA, 7190006 Santiago, Chile

Published online: 01 July 2020

grain boundaries mostly crystallized into cubic symmetry during sintering. However, upon cooling the cubic structure of perovskites transforms to low symmetry phases such as rhombohedral, orthorhombic or tetragonal symmetries on cooling through the Curie temperature [20]. The reduced symmetry of the transformed phases leads to the possibility of the formation of different domains in alternating patterns to relieve stresses associated with constrained transformation strains or to minimize the electrostatic energy at the expense of increased interfacial energy associated with the domain boundaries [21]. When external forces are applied to such materials below their Curie temperature, non-linear behaviors as well as hysteresis in stress–strain curves known as ferroelastic behavior are observed, which is attributed to domain switching [22–24]. Similar to other perovskites with rhombohedral distortion, BFO phase transition to lower symmetry structure is accompanied by domain formation, which exhibits ferroelectric, ferromagnetic and ferroelastic behavior. There are a very limited number of studies on ferroelastic behavior of BFO [25] and the ferroelastic behavior in the term of stress–strain curve still need to be understood. In this work, we have performed the ferroelectric, ferroelastic, magnetism and multiferroic behavior for polycrystalline BFO disks and bars.

2 Experimental details

To prepare BFO by the conventional solid-state reaction method, an appropriate portion of Bi_2O_3 and Fe_2O_3 regents from Sigma Aldrich as starting materials were mixed and ground by using an agate mortar until a homogeneous mixture is formed. The mixture was calcined at 600 °C for 3 h. The calcined powders were uniaxially pressed (90 MPa) to form green disks ($D = 12$ mm and $t = 3$ mm) and rectangular bars (12 mm × 6 mm × 3 mm) which were subsequently sintered at 840 °C for 10 h with the heating and cooling rates of 60 °C/h and 30 °C/h, respectively. The surfaces of sintered bars were mirror-polished and paralleled by a modified diamond paste and annealed at 820 °C for 1 h. The average density of disks and bars measured by geometrical method was 6.3 ± 0.1 g/cm^3 (~24% porosity). Structural characterizations of sintered samples were characterized by X-ray diffraction by using a Bruker D8 diffraction system with CuK_α radiation ($\lambda = 1.5406$ Å) and Rietveld refinement of the XRD patterns was done by using General Structure Analysis System (GSAS) software. The surface morphology of the microcrystals was examined by the scanning electron microscopy (SEM, JEOL JSM-6700). Leakage current and ferroelectric responses were measured with a P-E loop tracer (Radiant Technologies, USA). The magnetocapacitance (MC) measurement studies were performed with LCR meter (HIOKI 3532-50, Japan) by applying a magnetic field that varied from 0 Oe to 7 kOe. The magnetic properties of the samples were measured with a vibrating-sample magnetometer (5 T mini-VSM from Cryogenic Ltd.). For the uniaxial compression tests, the prepared bars were placed between two alumina rods and the load was raised from 5 N (~0.4 MPa) to 25 and 40 MPa with loading and unloading rate of 120 N/min using the load cell (Xforce HP, maximum load of 5 kN) and the clip-on extensometer (DMS ProLine 2, 0.005 µm resolution) was used for displacement measurement.

3 Result and discussion

3.1 Structural analysis

Figure 1a shows the XRD pattern of a sintered and annealed BFO bar, which demonstrates the peaks corresponding to rhombohedral crystal structure of BFO and additional peaks related to the secondary phases such as $Bi_{25}FeO_{39}$ (*) and $Bi_2Fe_4O_9$ (#). Figure 1b shows the Rietveld refinement analysis by which the lattice parameters of BFO ($a = 5.5844$ Å, $b = 5.5844$ Å, $c = 13.869$ Å, $R_{wp} = 3.0\%$, $R_p = 1.4\%$, $\chi^2 = 3.0$) were obtained, which are in good agreement with other literature reports [2].

X-ray diffraction spectrum is also used to estimate the crystallite size of BFO samples by using Scherrer formula as follows:

$$D = k\lambda/\beta_{hkl}\cos\theta \quad (1)$$

where D refers to the crystallite size (nm), k is the boarding constant (0.94), λ is the wavelength of the X-ray Cu Kα radiation (1.5406 Å), β is the width at half maximum of the diffraction peaks (radian), and "θ" is the diffraction angle (degrees). Since the breadth of the Bragg peak is the combination of both instrumental and sample dependent effects, it is necessary to collect a diffraction pattern from the line broadening of a standard material such as silicon to determine the instrumental broadening [26, 27]. The instrumental corrected broadening β_{hkl} corresponding to the diffraction peak of BFO, which are estimated by using the relation:

$$\beta_{hkl} = \left(\beta_{hkl\ measured} - \beta_{hkl\ instrumental}\right)^{1/2} \quad (2)$$

The average crystallite size of 30 nm was obtained for the BFO sample.

3.2 Micrographs analysis

Figure 2a, b shows SEM images of the surface of sintered and annealed BFO bars. As it can be seen, the rectangular shaped micrograins are clearly visible. The grain length and width distributions are demonstrated in Fig. 2c, d based on

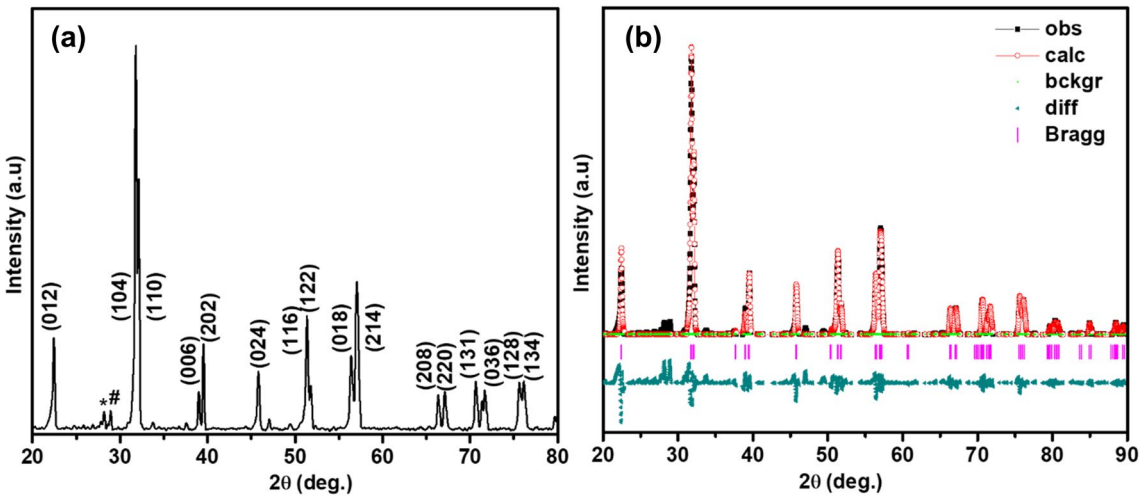

Fig. 1 **a** XRD pattern of sintered (840 °C/10 h) and annealed (820 °C/1 h) BFO bars, **b** Rietveld refinement of the X-ray diffraction data

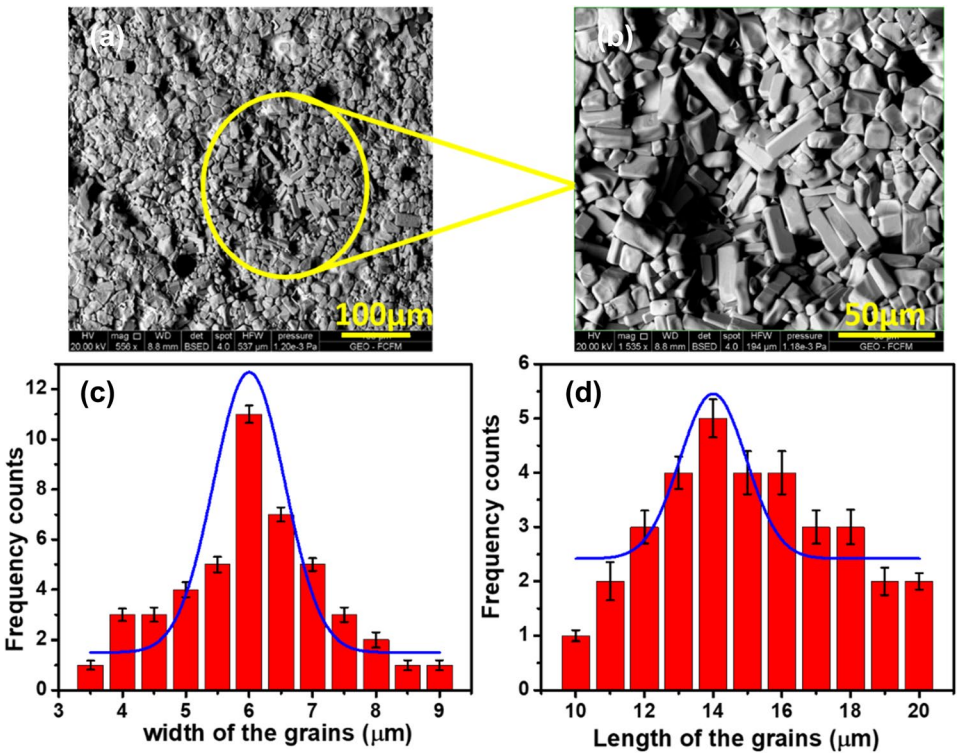

Fig. 2 **a** SEM images of sintered (840 °C/10 h) and annealed (820 °C/1 h) BFO bars, **b** magnified image of BFO, **c** grain size distributions width of the grains versus the number of grains, **d** grain size distributions length of the grains versus the number of grains

which the average grain width and length of 6 ± 0.42 μm and 14 ± 0.69 μm were calculated, respectively.

Figure 3 shows the high-resolution transmission electron micrograph of sintered BFO, which shows the full crystallinity of sintered samples as clear lattice fringes can be observed. The lattice fringes were measured with lattice spacing which were well matched with (012) of BFO which is in good agreement with inter-planar distance calculated from X-ray diffraction analysis.

3.3 Raman Studies

Figure 4 shows the Raman spectra measured in the range of 100–600 cm^{-1} at room temperature. As BFO has rhombohedral structure with the *R3c* space group with two formulas in one primitive cell, it has 18 optical phonon modes based on space group theory [2]:

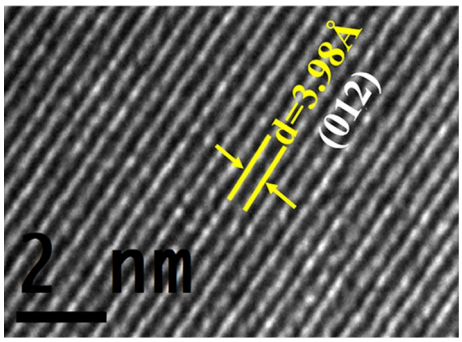

Fig. 3 HR-TEM micrograph of sintered (840 °C/10 h) and annealed (820 °C/1 h) BFO bar

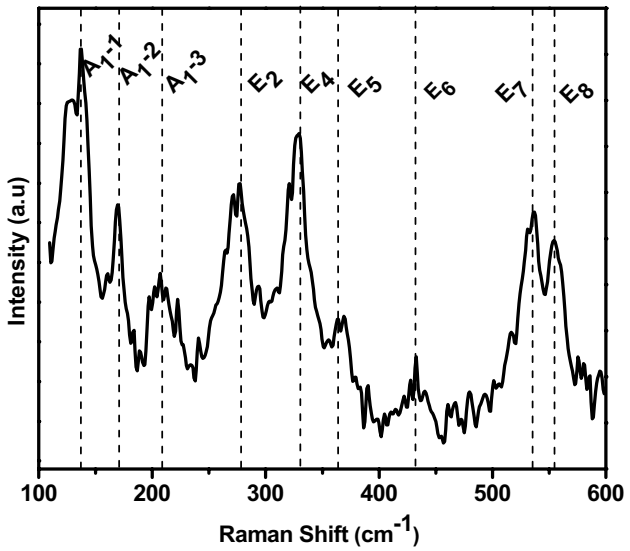

Fig. 4 Raman spectra for BFO ceramics in the range of 100–600 cm^{-1}

$$\Gamma_{\text{opt.}R3c} = 4A_1 + 5A_2 + 9E \quad (3)$$

where A_1 and E modes are Raman and infrared active modes which can be represented by

$$\Gamma_{\text{Raman},R3c} = 4A_1 + 9E \quad (4)$$

and A_2 modes are inactive modes [28] A_1 and E symmetry phonons are belonging to the longitudinal optical A_1 (LO) and transverse optical E (TO) phonon modes, respectively. In Raman scattering, the E modes can be observed by both parallel and crossed polarizations and the A_1 modes can be observed by only parallel polarization. Therefore, the E mode is related with the atomic motion in the plane of "*a*" and "*b*" while the A_1 mode is associated with the atomic motion along with the "*c*" axis. These observations of Raman modes are summarized in the Table 1 and compared with other reports in the literature [2, 29]

They show the strong Raman modes peaks of A_1-1, A_1-2, and A_1-3 modes appear at 138, 170, and 214 cm^{-1} and other weak E Raman modes peaks are E_2, E_4, E_5, E_6, E_7, E_8 which correspond to the 277, 330, 371, 432, 533, and 555 cm^{-1}, respectively. According to Muneeswaran et al. [2] and Yang et al. [29], the E_1, A_1-1, A_1-2, A_1-3, and E_2 modes are the characteristic phonon modes associated with the alteration of Bi-O covalent bonds, which may be attributed to the stereo chemical activity of Bi lone electron in the BFO and they are responsible for the inducing ferroelectric nature of the BFO. However, the obtained Raman modes are slightly shifted from the corresponding reported values, which may be due to preparation of BFO in various synthesis conditions and Bi deficiency during sintering.

3.4 Dielectric constant and dielectric loss measurements

Dielectric constant and dielectric loss of BFO disks as a function of frequency in the range from 100 Hz to 1 MHz at room temperature are shown in Fig. 5a. The values of real dielectric constant and loss factor are 194 and 3.6, respectively, for 1 kHz at room temperature. As it can be seen, they decrease gradually with increasing frequency up to 80 kHz and then became almost constant up to 1 MHz. These kinds of dielectric behaviors are expected from a ferroelectric material. The fundamental concept of these results shows the main role play in the different types of polarization like space charges, ionic defects, dipoles and atomic polarization. However, the behavior at lower frequency is attributed to the space charge polarization and that at higher frequency is ascribed to the ionic, dipole, and atomic polarizations.

Table 1 Observed and reported Raman modes for BFO samples

Raman modes (cm^{-1})	Muneeswaran et al. [2]	Yang et al. [29]	Present study
A_1-1	138	139	138
A_1-2	170	172	170
A_1-3	214	217	210
A_1-4	470	470	–
E_1	254	262	–
E_2	276	275	277
E_3	–	307	–
E_4	342	345	330
E_5	–	396	371
E_6	418	429	432
E_7	523	521	530
E_8	557	–	555
E_9	603	615	–

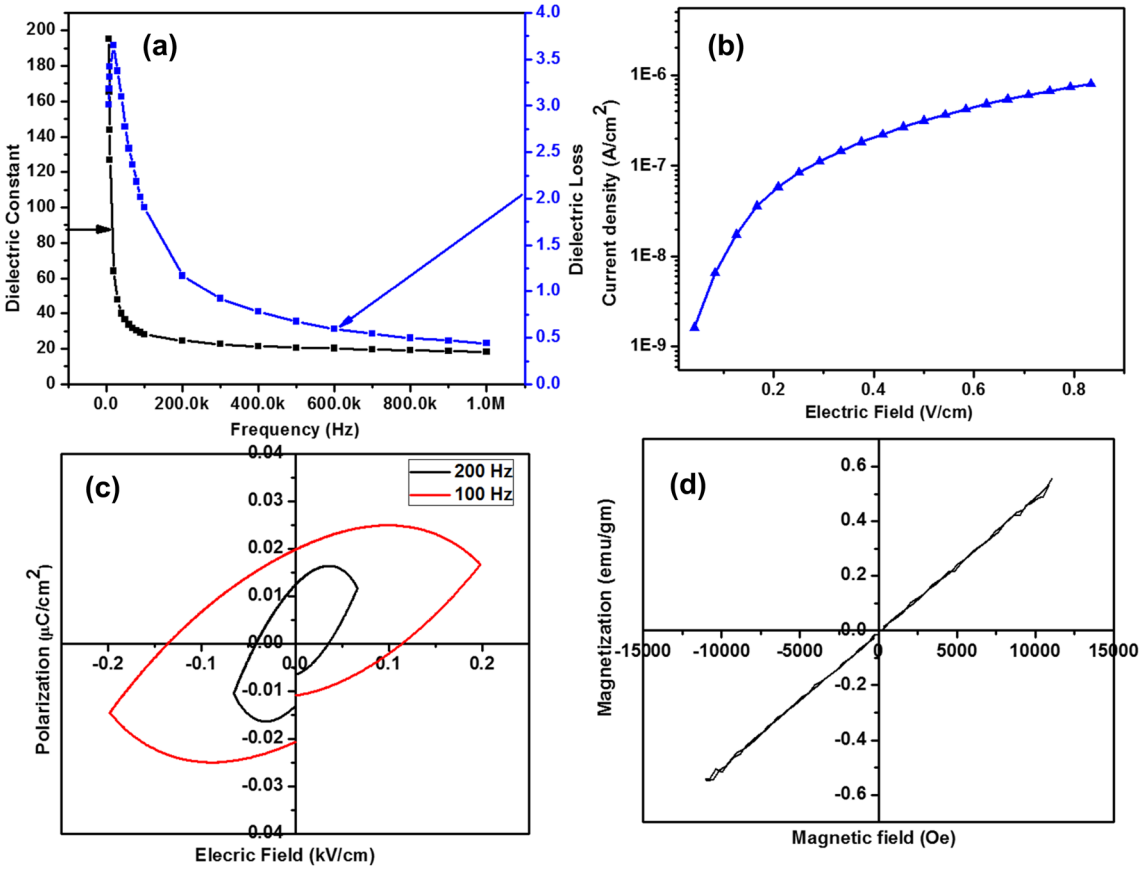

Fig. 5 **a** Frequency-dependent dielectric constant and dielectric loss, **b** *J–E* characteristics, **c** Polarization measured with applied electric field P-E loop for the prepared BFO disk at room temperature and **d** magnetization measured with applied magnetic field (*M–H* curve) for the prepared BFO bars measured at room temperature

When the frequency increases, the relative effect of ionic conductivity becomes small and as a result, the frequency dependence of dielectric constant becomes weak [30]. The high value of dielectric constant may also be attributed to size of the different grains in BFO [31].

3.5 Leakage current density

Figure 5b shows the leakage current density measured with different applied electric field (*J–E* curve) for BFO sintered disk, which shows a high leakage current density due to the space charges such as oxygen vacancies mainly induced by Bi volatilization. By the creation of oxygen vacancy into BFO samples, the electrons are trapped in centers which are readily activated for the conductivity by applied electric filed so that the leakage current density of the sample increases [32]. As the conductivity analysis plays the main role in the oxide based multiferroic materials, the leakage current density versus electric field (*J–E*) measurement of BFO ceramics at room temperature were studied. Leakage current density of 8.07×10^{-7} A/cm^2 and 1.54×10^{-9} A/cm^2 was obtained at higher and lower electric fields, respectively, which are similar with those reported for BFO bulk ceramics and thin films [33, 34]

There are two reasons for the higher leakage current density for BFO: (i) bismuth volatilization during high temperature sintering and (ii) creation of oxygen vacancies, which may be due to the Fe^{3+} to Fe^{2+} reduction [35]. If Fe^{3+} is reduced to Fe^{2+}, the system can then compensate ionically by forming oxygen vacancies ($V_O^{\bullet\bullet}$) or electronically with holes (h•). This oxygen vacancy formation can be derived by Kröger–Vink notation [36] to describe the electrical charge and lattice position for point defect species in composite samples:

$$2Fe_{Fe}^{x} + O_{o}^{x} \rightarrow 2Fe_{Fe}' + V_{o}^{\bullet\bullet} + \tfrac{1}{2}\,O_{2(g)} \quad (5)$$

$$Fe_{Fe}^{x} \rightarrow Fe_{Fe}' + h^{\bullet} \quad (6)$$

As demonstrated in above equations, the generated electronic charge carriers contribute to the leakage current density. It has been generating the electronic charge carriers

that contribute to leakage current density. In the present work, it seems that the higher leakage current density is due to bismuth deficiency as result of the impurity phase like $Bi_{25}FeO_{39}$, $Bi_2Fe_4O_9$ formations along with BFO.

3.6 P–E loop measurement

Figure 5c shows the polarization measured as a function of applied electric field with two different frequencies, which show ferroelectric hysteresis (P–E) loops for BFO disk. It has been observed that both P–E loops could not be fully saturated, which may be due to higher leakage current density in the samples. The obtained maximum remnant polarization (P_r) values are around 0.0120 and 0.0198 μC/cm^2 for low and high frequencies, respectively. However, it can be observed from the hysteresis loop that the values of remnant polarization and coercive fields decrease with increasing frequency. At lower frequency, electron displacement, ion displacement, turning-direction and space charge polarization contributes to the polarization of the sample. But, as the frequency increases, the space charge polarization cannot keep up with the change of electric field so the remnant polarization and coercive field values are decreased [37]. The obtained low remnant polarization and high coercive field may be due to the leakage current density in the samples, which is responsible for unsaturated P–E loop in BFO.

3.7 M–H loop measurement

Figure 5d shows the measured magnetization of BFO as a function of applied magnetic field at room temperature. A linear hysteresis loop was traced, which may be attributed to the G-type antiferromagnetic (AFM) nature of BFO. The saturated magnetic moment of 0.5 emu/gm was obtained, which is consistent with the magnitude of AFM in BFO. A similar result was reported for bulk BFO ceramic samples [38, 39]. However, Wang et al. [38] reported that the BFO has AFM magnetic structure with the G-type of spin ordering below T_N, and also this G-type of AFM structure has been modified by a cycloidal spin spiral with a large period of $\lambda = 620 \pm 20$ Å that is incommensurate with the lattice parameter.

3.8 Ferroelastic hysteresis loop measurement

The ferroelastic behavior of the BFO was studied by measuring the stress–strain curves of BFO bars with different maximum uniaxial compression stresses as shown in Fig. 6. As it can be seen, BFO exhibits the typical mechanical behavior of a ferroelastic material as the stress–strain curves show a visible non-linearity in loading and unloading due to ferroelastic domains switching and switching back, respectively, and a clear hysteresis and remnant strains. In general, the

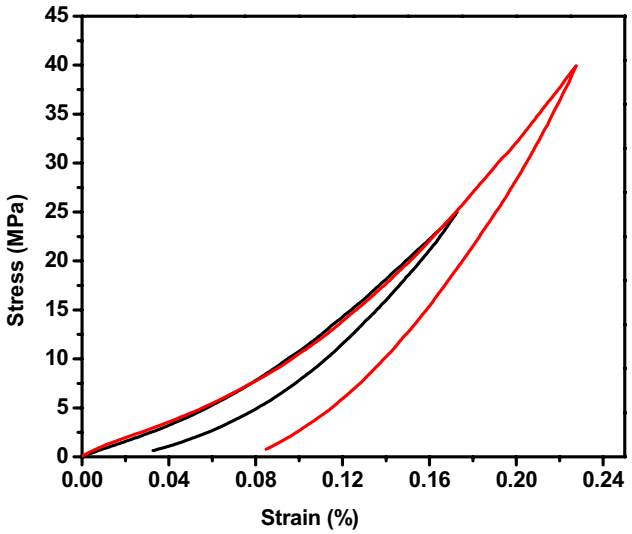

Fig. 6 The uniaxial compression stress–strain curves of sintered (840 °C/10 h) and annealed (820 °C/1 h) BFO bars for different maximum stresses

loading stress–strain curve of the ferroelastic materials can be divided in three initial, switching and loading parts: at the beginning of loading, the stress increases almost linearly with the strain and reaches to a critical stress where domain switching process starts and strain increases progressively in a plateau region, then the stress increases again when domain saturation occurs [23, 40, 41]. The obtained stress–strain curves of BFO bars almost start with switching plateau as the critical stress is very low ($\sigma_c \leq 5MPa$) due to having porosity (~ 24%) in the microstructure of the prepared samples as it has been reported that the porosity strongly affects ferroelastic behavior [42, 43]

It seems that the porosity facilitates domain nucleation due to providing more domain nucleation sites on free surface of the pores [44]. Also, having pores limited the fracture strength of samples [43] so that applying higher maximum stresses were not possible. To the best of our knowledge, there is no data available in the literature for the stress–strain curve of BFO for the sake of comparison. Sen et al. [45] reported elastic modulus of BFO obtained by nanoindentation, which depends on nanoindentation loads and attributed to elastic recovery and plastic deformation energy concepts and ferroelasticity of BFO was not considered. Alsubaie et al. [25] investigated effect of uniaxial tensile strain on motion of ferroelastic domains in BFO thin films by using bending experiment and found that the ferroelastic domains with in-plane polarization along the direction of applied tensile strain undergo expansion at the expense of neighboring domains and they completely revert to their pristine state on release of the applied mechanical strain. However, it has been shown that ferroelastic domains switch in $BaTiO_3$

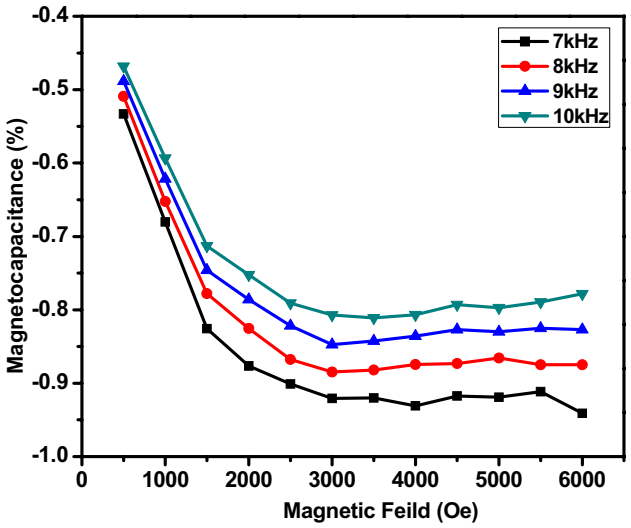

Fig. 7 Magnetocapacitance versus magnetic field measurement of BFO ceramics at room temperature

single crystals [46] and in PZT ceramics [47] under compressive stress where loading direction is influencing factor on the severity of domain switching. As it can be seen in Fig. 6, the remnant strains after unloading increases with increasing maximum applied stress, which can be attributed to incomplete switch-back of ferroelastic domains due to mechanical constraint or interlock of the more complex domain structure in tortuous pore and polycrystalline structure of BFO samples.

3.9 Magnetocapacitance measurement

In order to explain the magnetoelectric effect, the capacitance with different frequency was measured as a function of different applied magnetic field at room temperature as shown in Fig. 7. The origin of magnetoelectric effect is that the material will be strained when a multiferroic material is placed in a magnetic field and then generate an electric field on the ferroelectric domains; thus, it modifies the dielectric behavior of the samples due the existence of coupling between ferroelectric and magnetic domains. Magnetoelectric effect is measured in terms of magnetocapacitance and defined as:

$$Magneto-capacitance = \frac{Cp(H) - Cp(0)}{Cp(0)} 100(\%) \qquad (7)$$

where C_P (0) and C_P (H) are the capacitance in zero magnetic field and in the presence of magnetic field, respectively.

The obtained results can be explained by the capacitance measured with different frequencies like 7–10 kHz with applied magnetic field. It has been observed that the value of capacitance increases with increasing applied magnetic field and frequency, which can be attributed to the existence of coupling between magnetic and ferroelectric domains, which modifies the dielectric behavior of the samples [48].

4 Conclusions

In summary, BFO samples have been synthesized by a solid-state reaction and sintered at 840 °C for 10 h, which showed a rhombohedral structure with the space group of *R3c*. From Raman spectra, we observed (E_1, A_1-1, A_1-2, A_1-3, and E_2) Raman modes which are characteristic phonon modes and are associated with the alteration of Bi-O covalent bonds, which may be due to the stereo chemical activity of Bi lone electron in the BFO samples. The value of the real dielectric constant was found to be about 194 for 1 kHz and loss factor in the range of 3.6 at room temperature. The leakage current density was found to be 8.07×10^{-7} A/cm^2 and 1.54×10^{-7} A/cm^2 at higher and lower electric fields, respectively. From ferroelectric hysteresis loops of BFO disks, it has been observed that the values of remnant polarization and coercive fields decrease with increasing the frequency. Magnetic measurements show that the BFO bulk samples demonstrate the antiferromagnetic behavior at room temperature. The uniaxial compression stress–strain curves with different maximum loads showed hysteresis loop and remnant strain due to the ferroelastic behavior of BFO. Furthermore, the magnetoelectric coupling, measured in terms of magnetocapacitance which increases as the frequency increases, which indicates the existence of magnetoelectric coupling in the BFO ceramics.

Acknowledgements The authors acknowledge FONDECYT Postdoctoral Research Project No. 3180055, Government of Chile, for the financial support.

References

1. N.A. Hill, Why are there so few magnetic ferroelectrics? J. Phys. Chem. B. **104**, 6694–6709 (2000)
2. M. Muneeswaran, P. Jegatheesan, M. Gopiraman, I.S. Kim, N.V. Giridharan, Structural, optical, and multiferroic properties of single phased $BiFeO_3$. Appl. Phys. A. **114**, 853–859 (2014)
3. T. Kimura, T. Goto, H. Shintani, K. Ishizaka, T. Arima, Y. Tokura, Magnetic control of ferroelectric polarization. Nature **426**, 55–58 (2003)
4. J. Mundy, D.A. Muller, P. Schiffer, J.C. Fennie, R. Ramesh, W.D. Ratcliff, J.A. Borchers, A. Scholl, E. Arenholz, Atomically engineered ferroic layers yield a room-temperature magnetoelectric multiferroic. Nature **537**, 523–527 (2016)
5. B.B. Van Aken, T.T. Palstra, A. Filippetti, N.A. Spaldin, The origin of ferroelectricity in magnetoelectric $YMnO_3$. Nat. Mater. **3**, 164–170 (2004)
6. C. Fennie, Magnetic and electric phase control in epitaxial. Phys. Rev. Lett. **97**, 267602 (2006)

7. R. Seshadri, N.A. Hill, Visualizing the role of Bi 6s "Lone Pairs" in the Off-center distortion in ferromagnetic $BiMnO_3$. Chem. Mater. **13**, 2892–2899 (2001)
8. J. Wang, J.B. Neaton, H. Zheng, V. Nagarajan, S.B. Ogale, B. Liu, D. Viehland, V. Vaithyanathan, D.G. Schlom, U.V. Waghmare, N.A. Spaldin, K.M. Rabe, M. Wuttig, R. Ramesh, Epitaxial $BiFeO_3$ multiferroic thin film heterostructures. Science **299**, 1719 (2003)
9. T.T. Carvalho, P.B. Tavares, Synthesis and thermodynamic stability of multiferroic $BiFeO_3$. Mater. Lett. **62**, 3984–3986 (2008)
10. S.M. Selbach, A. Einarsrud, T. Grande, On the thermodynamic stability of $BiFeO_3$. Chem. Mater. **21**, 169–173 (2009)
11. Z. Liu, S. Liang, S. Li, Y. Zhu, X. Zhu, Synthesis, microstructural characterization, and dielectric properties of $BiFeO_3$ microcrystals derived from molten salt method. Ceram. Int. **41**, S19–25 (2015)
12. S.K. Pradhan, B.K. Roul, Improvement of multiferroic and leakage property in monophasic $BiFeO_3$. Phys. B **406**, 3313–3317 (2011)
13. P. Bai, Y. Zeng, J. Hana, Y. Wei, M. Li, Influence of Al doping on structural, dielectric, and ferroelectric properties of multiferroic $BiFeO_3$ ceramics. Ceram. Inter. **45**, 7730–7735 (2019)
14. Z.X. Cheng, A.H. Li, X.L. Wang, S.X. Dou, K. Ozawa, H. Kimura, S.J. Zhang, T.R. Shrout, Structure, ferroelectric properties, and magnetic properties of the La-doped bismuth ferrite. J. Appl. Phys. **103**, 07E507 (2008)
15. A. Kumar, P. Singh, R. Janay, D. Pandey, Effect of Mn-doping on the low temperature magnetic phase transitions of $BiFeO_3$. J. Alloys Compd. **825**, 154148 (2020)
16. V.A. Khomchenko, I.O. Troyanchuk, D.V. Karpinsky, Structural and magnetic phase transitions in $Bi_{1-x}Pr_xFeO_3$ perovskites. J. Mater. Sci. **47**, 1578–1581 (2012)
17. A. Agarwal, P. Aghamkar, V. Singh, O. Singh, A. Kumar, Structural transitions and multiferrocity in Ba and Co substituted nanosized bismuth ferrite. J. Alloy. Comp. **697**, 333–340 (2017)
18. S.G.N. Sinha, G.R. BinayKumar, Combined structural, electrical, magnetic and optical characterization of bismuth ferrite nanoparticles synthesized by auto-combustion route. Asian Ceram. Soc. **2**, 416–421 (2014)
19. Y. Xu, Y. Gao, H. Xing, J. Zhang, Room temperature spontaneous exchange bias in $BiFeO_3$ micro/nano powders synthesized by hydrothermal method. Ceram. Int. **44**, 17459–17463 (2018)
20. M. Johnsson, P. Lemmens, Crystallography and Chemistry of Perovskites. Handb. Magn. Adv. Magn. Mater. (2007). https://doi.org/10.1002/9780470022184.hmm411
21. S.K. Streiffer, C.B. Parker, A.E. Romanov, M.J. Lefevre, L. Zhao, J.S. Speck, W. Pompe, C.M. Foster, G.R. Bai, Domain patterns in epitaxial rhombohedral ferroelectric films. I. Geometry and experiments. J. Appl. Phys. **83**, 2742–2753 (1998)
22. E.K.H. Salje, Ferroelastic materials. Ann. Rev. Mater. Res. **42**, 265–283 (2012)
23. W. Araki, J. Malzbender, Ferroelastic deformation of $La_{0.58}Sr_{0.4}Co_{0.2}Fe_{0.8}O_{3-\delta}$ under uniaxial compressive loading. J. Eur. Ceram. Soc. **33**, 805–812 (2013)
24. A. Keitsiro, Possible species of ferromagnetic, ferroelectric, and ferroelastic crystals. Phys. Rev. B. **2**, 754 (1970)
25. A. Alsubaie, P. Sharma, J.H. Lee, J.Y. Kim, C.H. Yang, J. Seidel, Uniaxial strain controlled ferroelastic domain evolution in $BiFeO_3$. ACS Appl. Mater. Interfaces **10**, 11768–11775 (2018)
26. B.D. Cullity, *Elements of X-ray Diffraction*, 2nd edn. (Addison-Wesley, Boston, 1978)
27. J.I. Langford, A.J.C. Wilson, Scherrer after sixty years: a survey and some new results in the determination of crystallite size. J. Appl. Cryst. **11**, 102–113 (1978)
28. R. Haumont, J. Kreisel, P. Bouvier, F. Hippert, Phonon anomalies and the ferroelectric phase transition in multiferroic $BiFeO_3$. Phys. Rev. B **73**, 132101 (2006)
29. Y. Yang, J.Y. Sun, K. Zhu, Y.L. Liu, J. Chen, X.R. Xing, Raman study of $BiFeO_3$ with different excitation wavelengths. Phys. B **404**, 171–174 (2009)
30. M. Muneeswaran, P. Jegatheesan, N.V. Giridharan, Synthesis of nanosized $BiFeO_3$ powders by co-precipitation method. J. Exp. Nanosci. **8**, 341–346 (2013)
31. C. Elissalde, J. Ravez, Ferroelectric ceramics: defects and dielectric relaxations. J. Mater. Chem. **11**, 1957–1967 (2001)
32. M. Muneeswaran, R. Dhanalakshmi, N.V. Giridharan, Effect of Tb substitution on structural, optical, electrical and magnetic properties of $BiFeO_3$. J. Mater. Sci. Mater. Electron. **26**, 3827–3839 (2015)
33. Q.H. Jiang, C.W. Nan, Z.J. Shen, Synthesis and properties of multiferroic La-modified $BiFeO_3$ ceramics. J. Am. Ceram. Soc. **89**, 2123–2127 (2006)
34. Z. Zhong, H. Ishiwara, Variation of leakage current mechanisms by ion substitution in $BiFeO_3$ thin films. Appl. Phys. Lett. **95**, 112902 (2009)
35. M. Muneeswaran, J.W. Jang, J.H. Jeong, A.A. Fakhrabadi, N.V. Giridharan, Effect of dopant-induced defects on structural, electrical, and enhanced ferromagnetism and magnetoelectric properties of Dy and Sr co-doped $BiFeO_3$. J. Mater. Sci. Mater. Electron. **30**, 7359–7366 (2019)
36. F.A. Kroger, H.J. Vink, in *Solid State Physics*, ed. by F. Seitz, D. Turnbull (Academic Press, New York, 1956), p. 307
37. W. Cai, C. Fu, W. Hu, G. Chen, X. Deng, Effects of microwave sintering power on microstructure, dielectric, ferroelectric and magnetic properties of bismuth ferrite ceramics. J. Alloys Compd. **554**, 64–71 (2013)
38. Y.P. Wang, G.L. Yuan, X.Y. Chen, J.M. Liu, Z.G. Liu, Electrical and magnetic properties of single-phased and highly resistive ferroelectromagnet $BiFeO_3$ ceramic. J. Phys. D: Appl. Phys. **39**, 2019 (2006)
39. M. Muneeswaran, S.H. Lee, D.H. Kim, B.S. Jung, S.H. Chang, J.W. Jang, B.C. Choi, J.H. Jeong, N.V. Giridharan, C. Venkateswaran, Structural, vibrational, and enhanced magnetoelectric coupling in Ho-substituted $BiFeO_3$. J. Alloys Compd. **750**, 276–285 (2018)
40. W. Araki, K. Takeda, Y. Arai, Mechanical behaviour of ferroelastic lanthanum metal oxides $LaMO_3$ (M=Co, Al, Ga, Fe). J. Eur. Ceram. Soc. **36**, 4089–4409 (2016)
41. T. Leist, K.G. Webber, W. Jo, T. Granzow, E. Aulbach, J. Suffner, J. Rodel, Domain switching energies: mechanical versus electrical loading in La-doped bismuth ferrite–lead titanite. J. Appl. Phys. **109**, 054109 (2011)
42. N. Islam, W. Araki, Y. Arai, Mechanical properties of ferroelastic $La_{0.6}Sr_{0.4}Co_{0.2}Fe_{0.8}O_{3-\Delta}$ with various porosities and pore sizes. J. Mater Sci. **54**, 5256–5265 (2019)
43. M.N. Islam, W. Araki, Y. Arai, Mechanical behavior of ferroelastic porous $La_{0.6}Sr_{0.4}Co_{0.2}Fe_{0.8}O_{3-\delta}$ prepared with different pore formers. Ceram. Int. **43**, 14989–14995 (2017)
44. G. Lu, S. Li, X. Ding, J. Sun, E.K.H. Salje, Ferroelectric switching in ferroelastic materials with rough surfaces. Sci. Rep. **9**, 1–7 (2019)
45. P. Sen, A. Dey, A.K. Mukhopadhyay, S.K. Bandyopadhyay, A.K. Himanshu, Nanoindentation behavior of nano $BiFeO_3$. Ceram. Int. **38**, 1347–1352 (2012)
46. J.M. Saldana, G.A. Schneider, L.M. Eng, Stress induced movement of ferroelastic domain walls in $BaTiO_3$ single crystals evaluated by scanning force microscopy. Surf. Sci **480**, L402–L410 (2001)

47. M. Okayasu, K. Bam, Domain switching characteristics of lead zirconate titanate piezoelectric ceramics on a nanoscopic scale. J. Eur. Ceram. Soc. **37**, 145–159 (2017)
48. B. Ruette, S. Zvyagin, A.P. Pyatakov, A. Bush, J.F. Li, V.I. Belotelov, A.K. Zvezdin, D. Viehland, Magnetic-field-induced phase transition in BiFeO3 observed by high-field electron spin resonance: cycloidal to homogeneous spin order. Phys. Rev. B. **69**, 064114 (2004)